Supplement to Low-volatility compounds contribute significantly to isoprene SOA under high-NO conditions

Rebecca H. Schwantes[1,5], Sophia M. Charan[2], Kelvin H. Bates[2,6], Yuanlong Huang[1], Tran B. Nguyen[3], Huajun Mai[1], Weimeng Kong[2], Richard C. Flagan[2], and John H. Seinfeld[2,4]

[1]Division of Geological and Planetary Sciences, California Institute of Technology, 1200 East California Boulevard, Pasadena, California 91125, United States
[2]Division of Chemistry and Chemical Engineering, California Institute of Technology, 1200 East California Boulevard, Pasadena, California 91125, United States
[3]Department of Environmental Toxicology, University of California - Davis, Davis, California 95616, United States
[4]Division of Engineering and Applied Science, California Institute of Technology, Pasadena, California 91125, USA
[5]Current Affiliation: National Center for Atmospheric Research, Boulder, Colorado, 80307, USA
[6]Current Affiliation: Faculty of Arts and Sciences, Harvard University, Cambridge, MA 02138, USA

Correspondence to: Rebecca H. Schwantes (rschwant@ucar.edu)

S1 Comparisons between Kinetic Model and Experimental Results

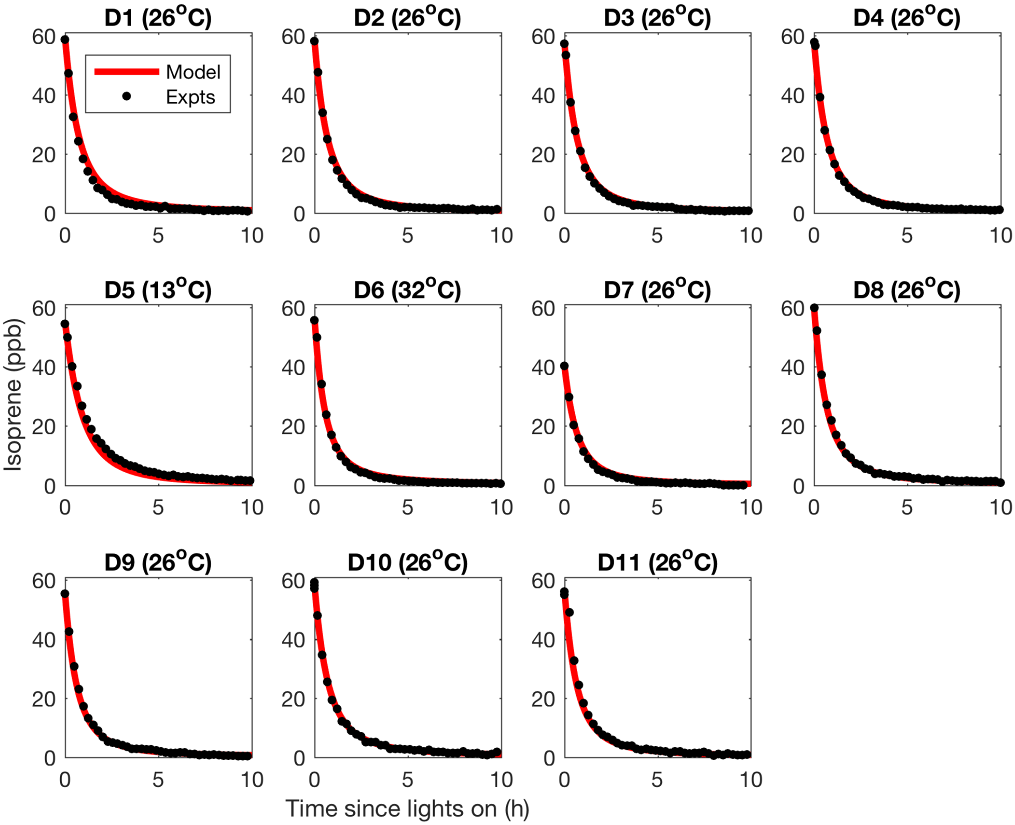

Figure S1. Isoprene observed (**black**) compared to simulated (**red**) for all LV (low volatility) pathway experiments.

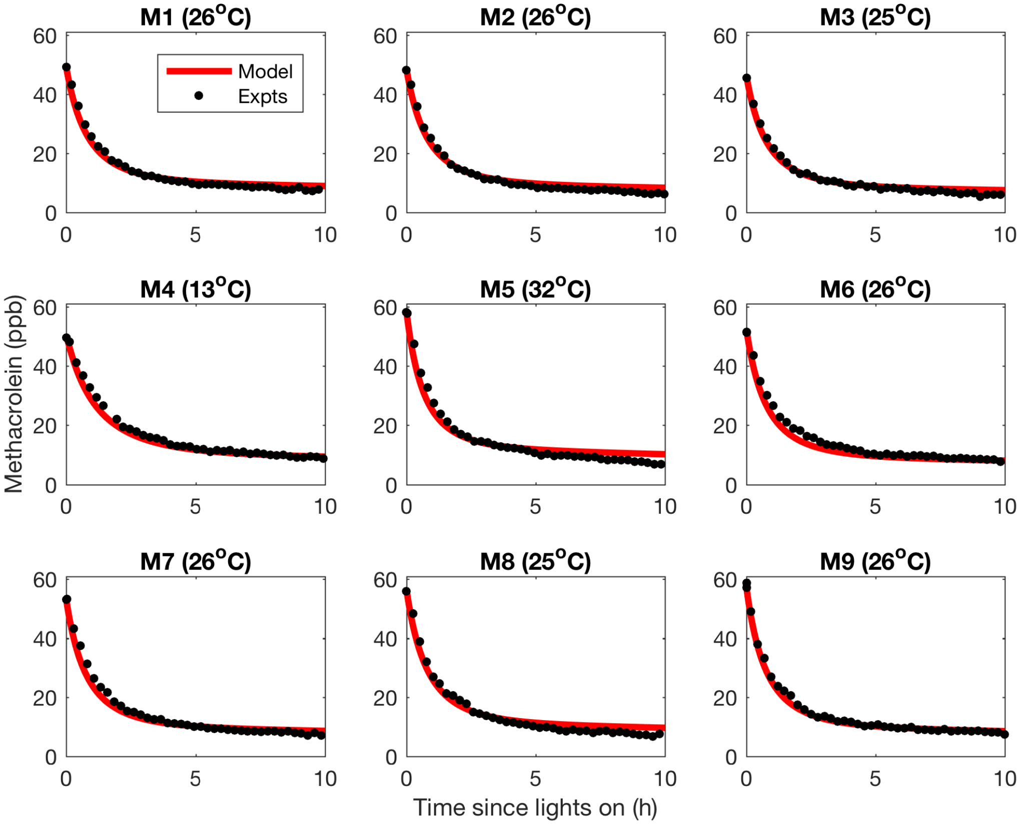

Figure S2. Methacrolein observed (**black**) compared to simulated (**red**) for all 2MGA (2-methyl glyceric acid and oligomers) pathway experiments.

As shown in Figure S3, NO_2 and NO compare reasonably well with the model in both the LV and 2MGA experiments. NO is measured using a Teledyne NO_x analyzer (T200) and NO_2 is measured using a luminol NO_2/acyl peroxynitrate analyzer developed by Fitz Aerometric Technologies. There is a large model bias in the NO_2/NO ratio (Figure S3), but this bias is largely caused by differences of only several ppb in the NO level between the model and observations. NO/NO_x and NO_2/NO_x are much more similar between the model and observations and are a more relevant metric for determining MPAN formation at high NO_2/NO ratios. Remaining biases are likely caused by unknown measurement interferences or unaccounted for wall deposition of NO_x reservoir species (e.g., N_2O_5, HNO_3, HO_2NO_2, etc.) in the kinetic model.

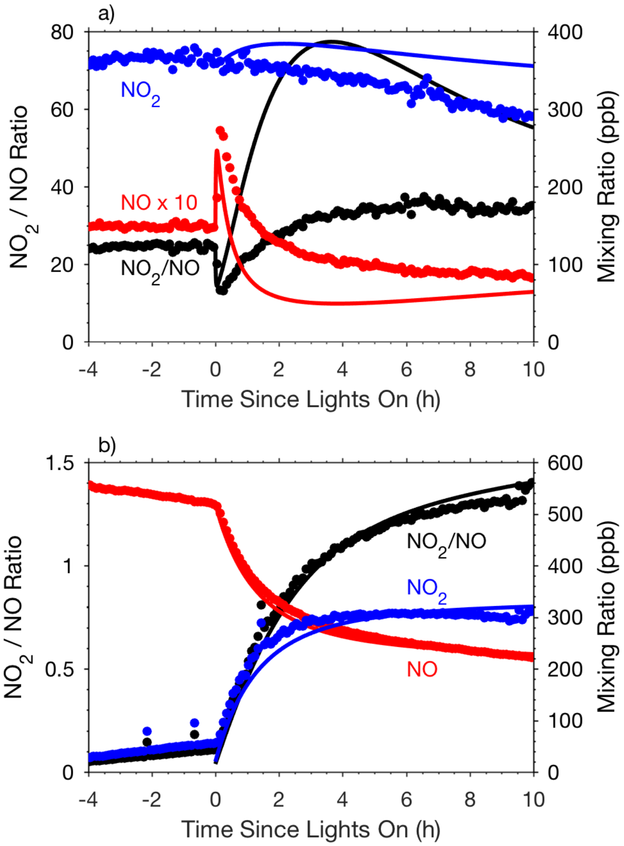

Figure S3. NO_2 (**blue**, right axis), NO (**red**, right axis), and NO_2 / NO ratio (**black**, left axis) for an example 2MGA experiment (M2, panel a) and an example LV experiment (D8, panel b) comparing experimental data (markers) and kinetic model results (lines). Note: in panel a, the NO mixing ratio is multiplied by 10 for ease of viewing.

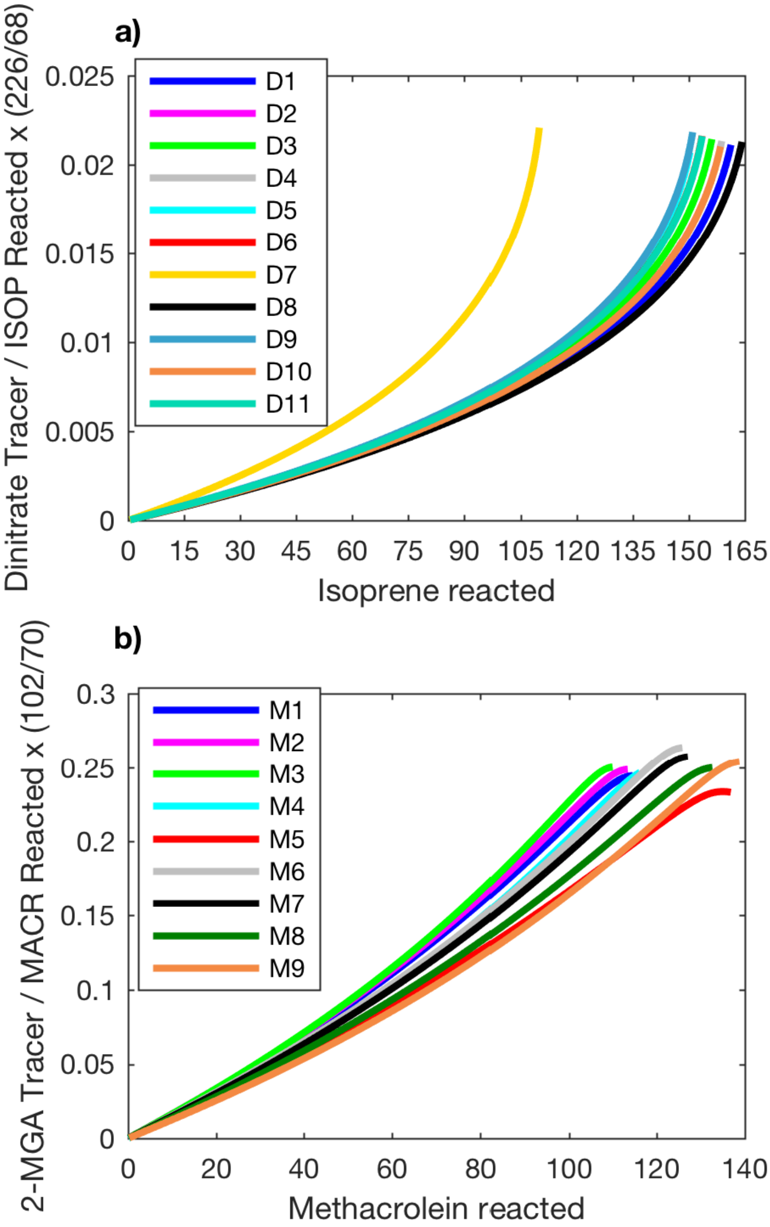

Figure S4. Simulated known gas-phase SOA precursors converted to a proxy of SOA yield for all LV pathway experiments (panel a) and all 2MGA pathway experiments (panel b). The kinetic model confirms experimental conditions were similar enough to produce relatively consistent yields of known gas-phase SOA precursors. The dinitrate and HMML gas-phase tracers were added into the chemical mechanism with no loss pathways (i.e, OH oxidation). OH oxidation of the dinitrates and HMML is slow enough that this has a minor impact on the results. The dinitrate tracer includes all dihydroxy dinitrates from isoprene and the 2-MGA tracer includes HMML + MAE.

S2 Corrections for Particle Coagulation and Particle Wall Deposition

For each experiment, after all gases and particles were injected into the chamber, purified air was added to facilitate mixing. Photooxidation was delayed by 4 h, during which particle wall deposition was measured. The first 0.5 h of this 4 h period was not used in the particle wall deposition calculation to ensure that air currents and particles/gases in the chamber had stabilized. A numerical model, similar to that reported by Nah et al. (2017), Sunol et al. (2018), and Charan et al. (2018) was used to simulate Brownian diffusion, particle settling, and electrostatic effects. The numerical model based on the aerosol dynamic equation (e.g., Sunol et al. (2018)) assumes β(D_p,t) follows the Crump and Seinfeld (1981) equation for a spherical chamber. Prior to injection, all ammonium sulfate particles were passed through a soft x-ray source (TSI Model 3088) in order to impart a consistent initial charge distribution with a net charge of zero. For the particle coagulation/wall deposition correction, the initial charge distribution was assumed to be that computed by Leppa et al. (2017), which is an update to Lopez-Yglesias and Flagan (2013) and Wiedensohler (1988) and consistent with the charge distribution assumed in the DMA inversion (Section 2.2 of the main text). Only charges from -8 to 8 are considered, which is sufficient for the particles used in this study, which have a diameter range of 30 - 800 nm. All particles measured by the DMA were grouped into 15 size bins. The DMA collects data across 390 size bins, but reducing the size bin number decreased the analysis uncertainty by increasing the number of particles per size bin. The only unknown parameters in the numerical model then become the mean electrostatic field experienced within the chamber ($\bar{E}$) and the chamber eddy diffusion coefficient (k_e). The numerical model determines k_e and $\bar{E}$ by comparing the observed particle dynamics to that simulated and minimizing the optimization function J.

$$J = \int_0^{t_{final}} \sum_{D_p} \left(\left(\sum_{charges} N(D_p, t; ke, \bar{E})_{simulated} - N(Dp, t)_{observed} \right)^2 \frac{N(D_p,t)_{observed}}{\sum_{D_p} N(D_p,t)_{observed}} \right) dt \qquad (1)$$

The particle wall deposition coefficients (β(D_p,t)) can then be extrapolated from k_e and $\bar{E}$. Tabulated k_e and $\bar{E}$ values for all experiments are provided in Table S1. Only experiments with an inferred chamber electric field within the range verified by the control experiments (i.e., $\bar{E}$ value < 15.7 V cm^{-1}) are reported. This consequently also removes experiments with abnormally high k_e values.

Table S1. Optimized mean electrostatic field experienced within the chamber ($\bar{E}$) and the eddy diffusion coefficient (k_e) for all experiments.

Experiment #	k_e (s^{-1})	$\bar{E}$ (V cm^{-1})
Control Dry Experiments		
C1	0.05	5.1
C2	0.10	8.9
C3	0.06	7.0
C4	0.21	15.7
Control Humid Experiments		
C5	0.07	7.9
C6	0.02	5.8
C7	0.11	11.8
C8	0.15	15.3
C9	0.31	20.9
Experiments optimized for LV pathway		
D1	NA	NA
D2	0.03	4.3
D3	0.03	5.6
D4	0.03	6.5
D5	0.27	13.3
D6	0.30	14.2
D7	0.02	4.5
D8	1.48	17.7
D9	1.09	27.6
D10	0.01	2.1
D11	0	0
Experiments optimized for 2MGA pathway		
M1	NA	NA
M2	0.29	11.6
M3	0.16	10.9
M4	0.32	10.6
M5	0.30	12.4
M6	1.02	18.7
M7	0.45	20.5
M8	0.33	19.6
M9	0	0

For experimental conditions, see Table 1 in main text.

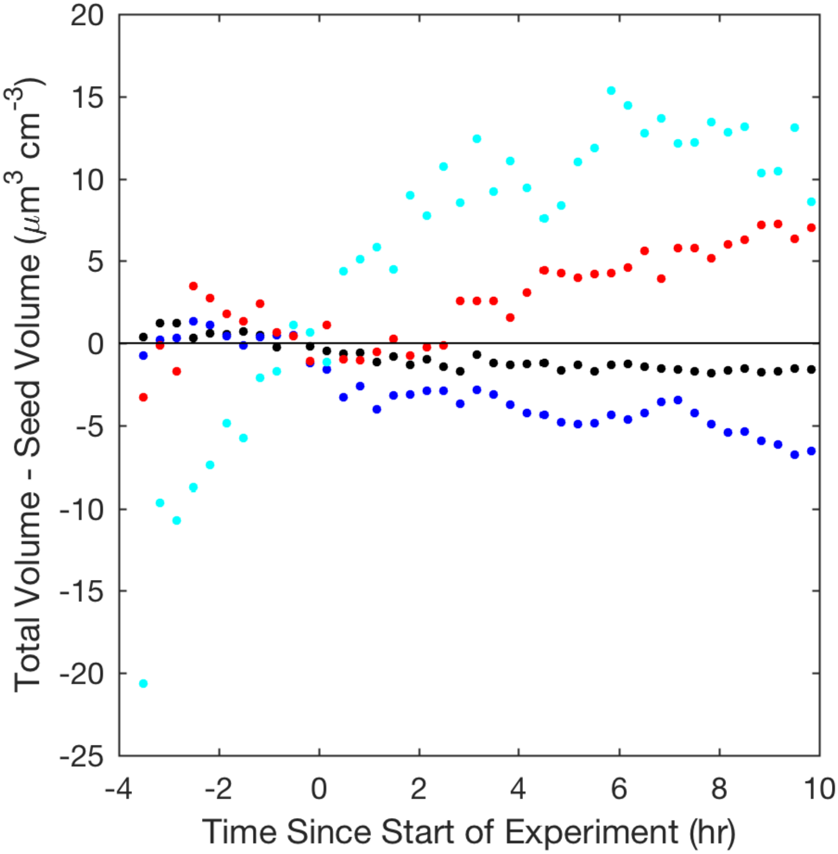

Figure S5. Total volume - seed volume (20 min averages) for the following particle wall deposition control experiments: C1 (V = 37 $\mu m^3 cm^{-3}$, ●), C2 (109 $\mu m^3 cm^{-3}$, ●), C3 (183 $\mu m^3 cm^{-3}$, ●), and C4 (375 $\mu m^3 cm^{-3}$, ●), respectively where V = initial corrected particle volume.

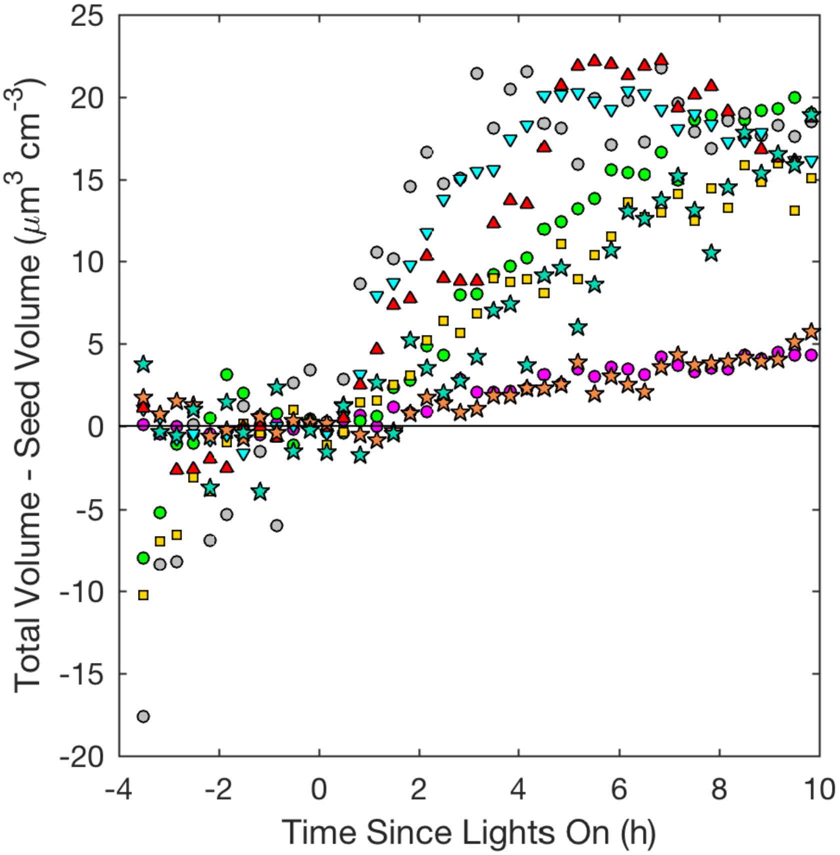

Figure S6. Total volume minus seed volume (20 min averages) as measured by DMA for all isoprene experiments with seed aerosol: seed surface area - D2 (SA = 1170 μm^2 cm^{-3}, ●), D3 (SA = 3420 μm^2 cm^{-3}, ●), & D4 (SA = 5770 μm^{2}cm^{-3}, ●), temperature - D5 (13 °C, ▼) and D6 (32 °C, ▲), isoprene loading - D7 (initial isoprene 110 μg m^{-3}, ♦), and new chamber with less wall charging - D10 (SA = 1580 μm^{2}cm^{-3}, ★) and D11 (SA = 4770 μm^{2}cm^{-3}, ★)

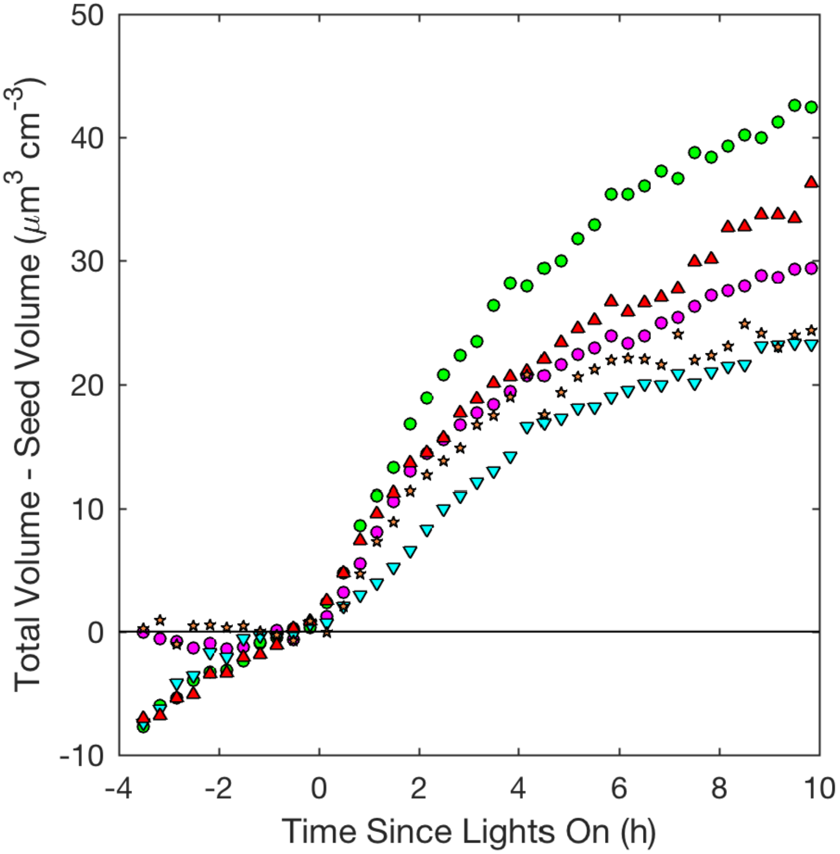

Figure S7. Total volume - seed volume (20 min averages) for all methacrolein experiments with seed aerosol: seed surface area - M2 (SA = 1640 μm^{2}cm^{-3}, ●), & M3 (SA = 2260 μm^{2}cm^{-3}, ●), temperature - M5 (13 °C, ▼) and M6 (32 °C, ▲), and new chamber with less wall charging - M9 (SA = 1910 μm^{2}cm^{-3}, ★).

S3 Additional Aerosol Composition Analysis from Aerosol Mass Spectrometer

The AMS results confirm that organic nitrates are present in the particle phase under dry conditions, but this technique is ill-suited for identifying specific organic nitrates present because $C_wH_xN_yO_z^+$ ions are produced in small yields (∼5% of the nitrogen signal and <1% of the organic signal) and often occluded by more abundant peaks (Farmer et al., 2010). Organic nitrates fragment with a distinctly higher NO^+ / NO_2^+ ratio than inorganic ammonium nitrate (Farmer et al., 2010). Considering ammonium nitrate fragments to an NO^+ / NO_2^+ ratio of 2.4 for the Caltech AMS, the NO^+ / NO_2^+ ratio of 4-8 (Figure S8) implies organic nitrates are present during all the LV and 2MGA pathway experiments performed under dry conditions. Under humid conditions, nitric acid partitions to the particle phase (Figure S8) and the NO^+ / NO_2^+ (∼2) shifts closer to that of ammonium nitrate.

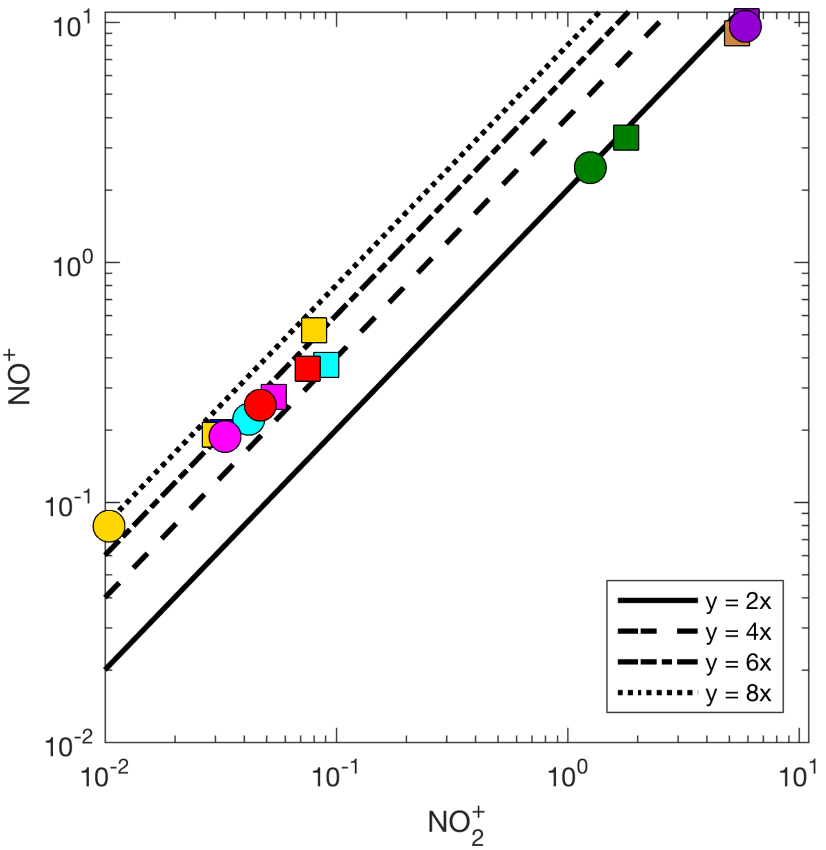

Figure S8. Average NO^+ vs NO_2^+ ratio from AMS during 10 h of photooxidation for LV pathway experiments (○) and 2MGA experiments (☐) with colors indicating no initial seed aerosol (**blue**), seed aerosol (**magenta**), 13°C (**cyan**), 32°C (**red**), RH ∼50% (**green**), RH ∼70% (**brown**), RH ∼80% (**purple**), new chamber with negligible wall charging (**gold**)

As explained in Section 4.1 of the main text, SOA mass yields measured by the DMA under humid conditions were not reported due to the need for more characterization of particle coagulation and wall loss under humid, high-NO, and high-nitric acid conditions. The AMS results can provide a qualitative understanding of the SOA mass formed under various conditions. Due to uncertainties in the collection efficiency (CE), the AMS results should not be used for quantification of SOA mass in chamber experiments. Because humidity will enhance the CE (e.g., Docherty et al., 2013), for all humid experiments a Nafion dryer was used to dry the particles prior to AMS measurement. Changes in the CE due to differences in the organic composition between the experiments are possible. The AMS results are not corrected for particle wall loss. Additionally, as explained in Section 5.2 of the main text, an interference due to ammonium sulfate (Pieber et al., 2016) was subtracted from the organic signal. In general, this interference was higher and more variable in the humid experiments than the dry experiments.

For the LV pathway experiments, increases in humidity increase the aerosol mass measured by the AMS (Figure S9a). Given the low collection efficiency for the LV pathway compared to that from the 2MGA pathway (Section 5.3 of the main text), this increase is likely explained by slight enhancements in the particle phase of compounds, to which the AMS is more sensitive such as glyoxal and methylglyoxal. Zhang et al. (2011) determined the isoprene high-NO SOA mass yield under dry conditions was $\sim$ 2 times larger than that under humid conditions. Dommen et al. (2006) determined the isoprene SOA yield was not dependent on RH from 2-85%; however, Zhang et al. (2011) reevaluated data from Dommen et al. (2006) and concluded that when comparing only experiments performed under similar conditions, the SOA mass yield under dry conditions is $\sim$2 times greater than that formed under humid conditions. Here when comparing the AMS results for experiments M6 (RH = 47%) and M2 (RH = 8.9%), which have similar initial seed surface areas, SOA formation under dry conditions is $\sim$ 1-2 times higher than under humid conditions depending on the time of oxidation (Figure S9b).

In Figures S11-S14 and 9-10 in the main text, the average AMS mass spectra over the entire experiment (10h of photooxidation) is shown. The contribution of the highlighted fragments to the total tend to be fairly consistent over the entire 10h photooxidation period in both the LV and 2MGA pathway experiments.

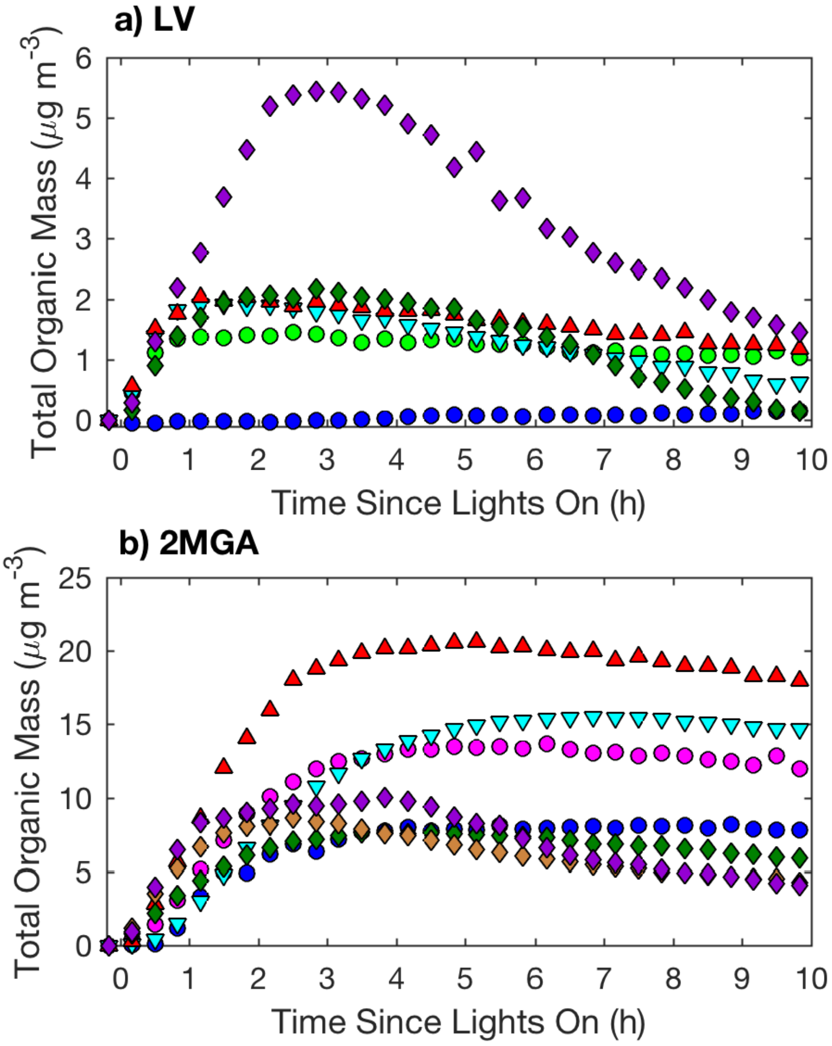

Figure S9. Total organic mass (20 minute averages) as measured by the AMS for LV pathway experiments (panel a): seed surface area - D1 (SA = 0 μm^2 cm^{-3}, ●) & D3 (SA = 3420 μm^2 cm^{-3}, ●), temperature - D5 (13 °C, ▼) & D6 (32 °C, ▲), and humidity - D8 (RH = 45%, ◆) & D9 (RH = 78%, ◆) and 2MGA pathway experiments (panel b): seed surface area - M1 (SA = 0 μm^2 cm^{-3}, ●) & M2 (SA = 1640 μm^2 cm^{-3}, ●), temperature - M4 (13 °C, ▼) & M5 (32 °C, ▲), and humidity - M6 (RH = 47%, ◆), M7(RH = 67%, ◆), & M8 (RH = 81%, ◆).

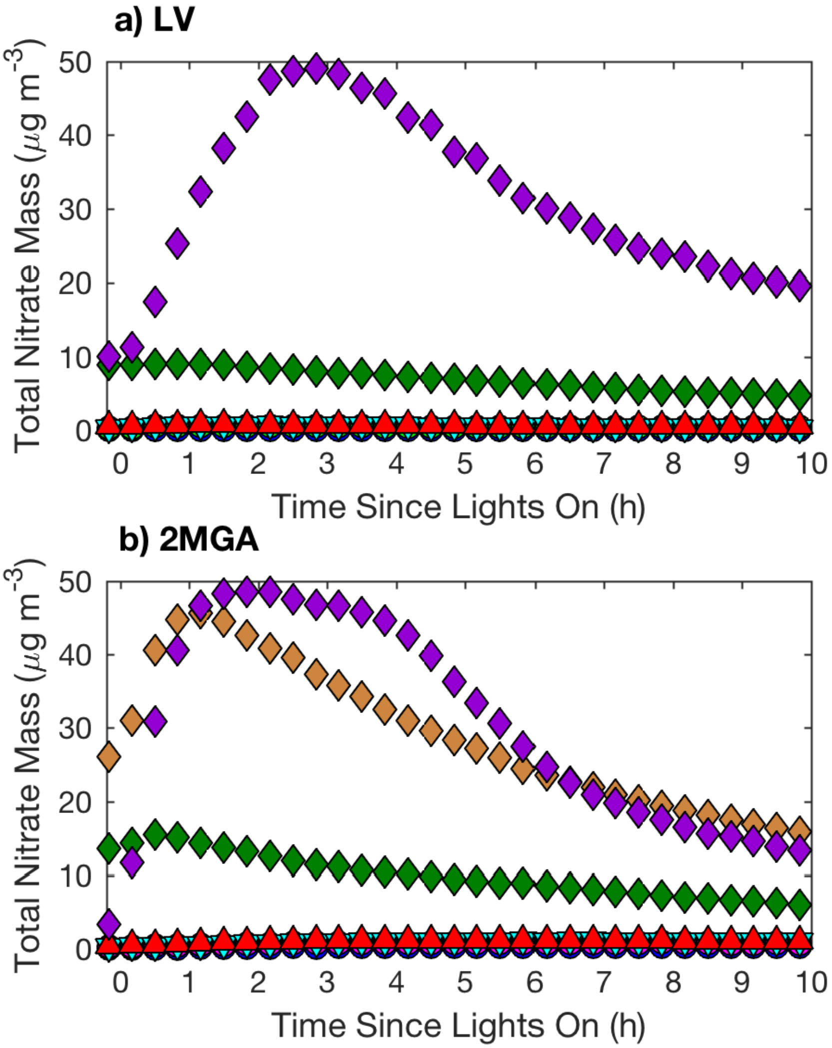

Figure S10. Total nitrate mass (20 minute averages) as measured by the AMS for LV pathway experiments (a): seed surface area - D1 (SA = 0 µm^2 cm^{-3}, ●) & D3 (SA = 3420 µm^2 cm^{-3}, ●), temperature - D5 (13 °C, ▼) & D6 (32 °C, ▲), and humidity - D8 (RH = 45%, ♦) & D9 (RH = 78%, ♦) and 2MGA pathway experiments (b): seed surface area - M1 (SA = 0 µm^2 cm^{-3}, ● & M2 (SA = 1640 µm^2 cm^{-3}, ●, temperature - M4 (13 °C, ▼) & M5 (32 °C, ▲), and humidity - M6 (RH = 47%, ♦), M7(RH = 67%, ♦), & M8 (RH = 81%, ♦).

a) LV - Low Temperature

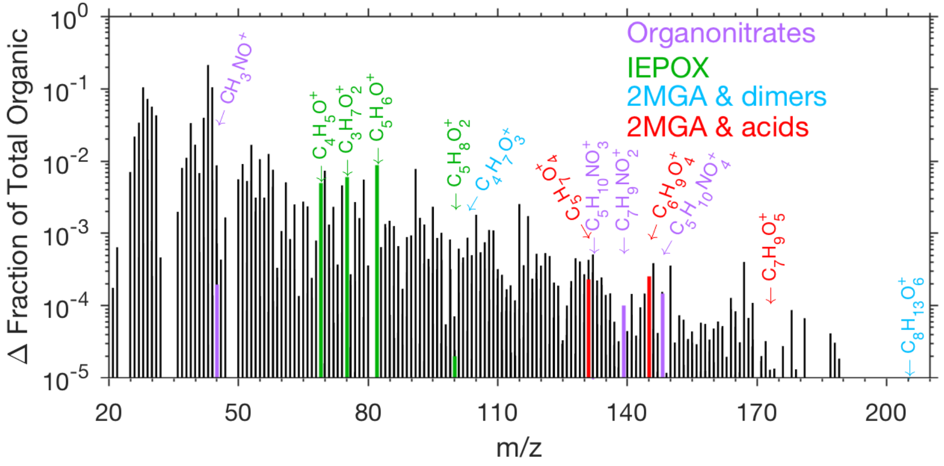

b) LV - High Temperature

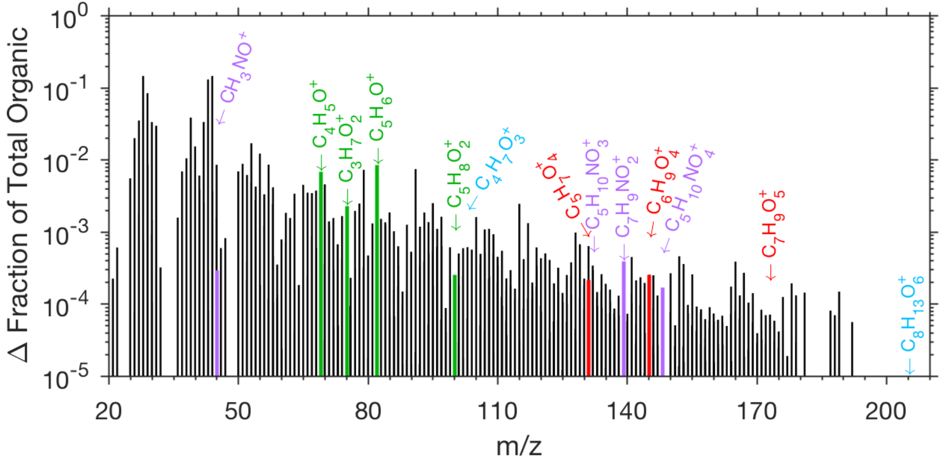

Figure S11. High resolution AMS mass spectra (averaged over 10h of photooxidation - the sulfate background) for experiment D5 (13 °C, panel a) and D6 (32 °C, panel b). Fragments are labeled as 2-MGA monomer/dimer (**cyan**), esterification of 2-MGA with acids (**red**), isoprene epoxydiol (IEPOX) tracers (**dark green**), and examples of organonitrate fragments - $C_xH_yNO_z$ (**purple**).

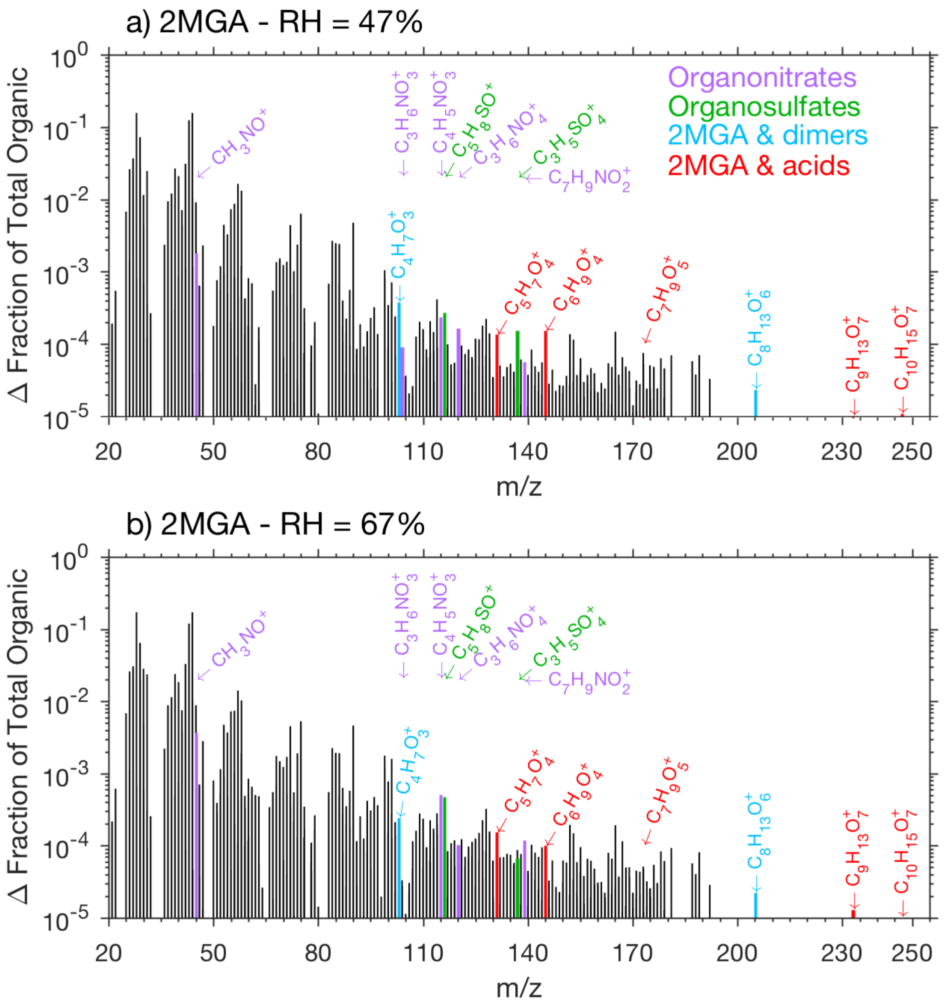

Figure S12. High resolution AMS mass spectra (averaged over 10h of photooxidation - the sulfate background) for experiment M6 (RH = 47%, panel a) and M7 (RH = 67%, panel b). Fragments are labeled as 2-MGA monomer/dimer (**cyan**), esterification of 2-MGA with acids (**red**), examples of organosulfate fragments (**dark green**), and examples of organonitrate fragments - $C_xH_yNO_z$ (**purple**).

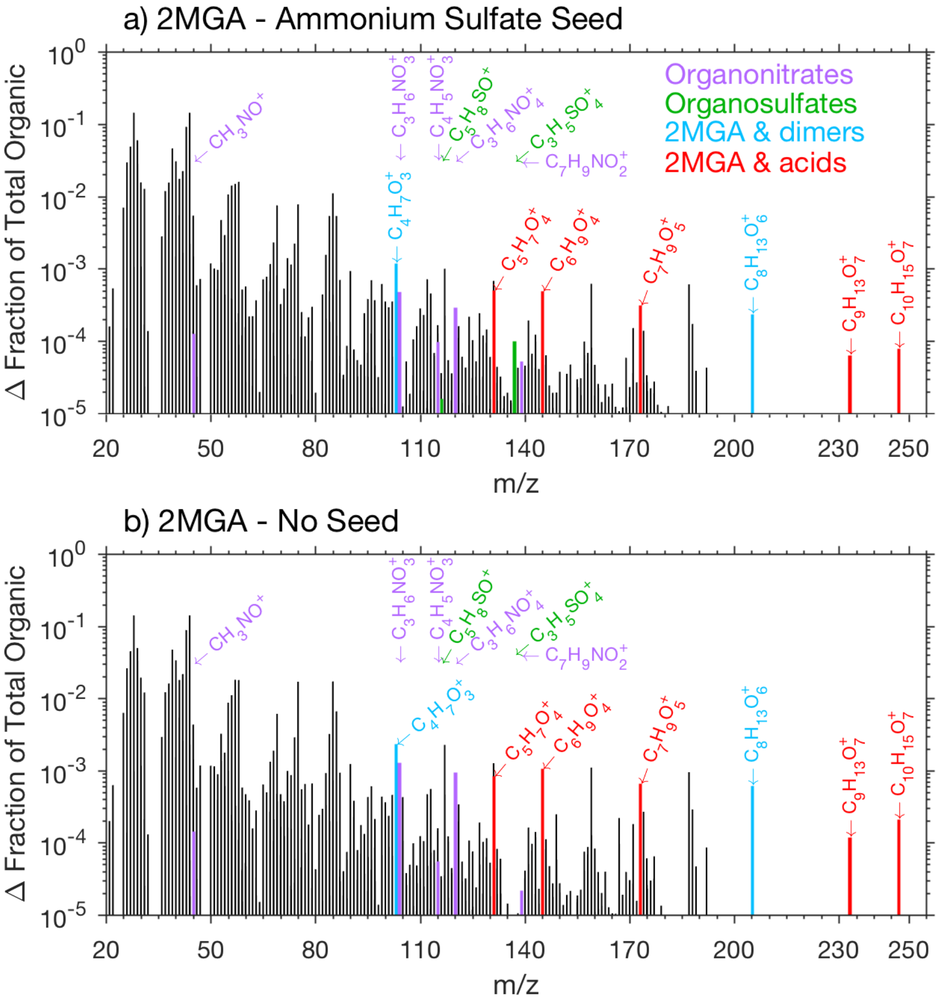

Figure S13. High resolution AMS mass spectra (averaged over 10h of photooxidation - the sulfate background) for experiment M2 (1640 $\mu m^2\ cm^{-3}$, panel a) and AMS mass spectra (averaged over 10h of photooxidation) for experiment M1 (0 $\mu m^2\ cm^{-3}$, panel b). Fragments are labeled as 2-MGA monomer/dimer (**cyan**), esterification of 2-MGA with acids (**red**), examples of organosulfate fragments (**dark green**), and examples of organonitrate fragments - $C_xH_yNO_z$ (**purple**).

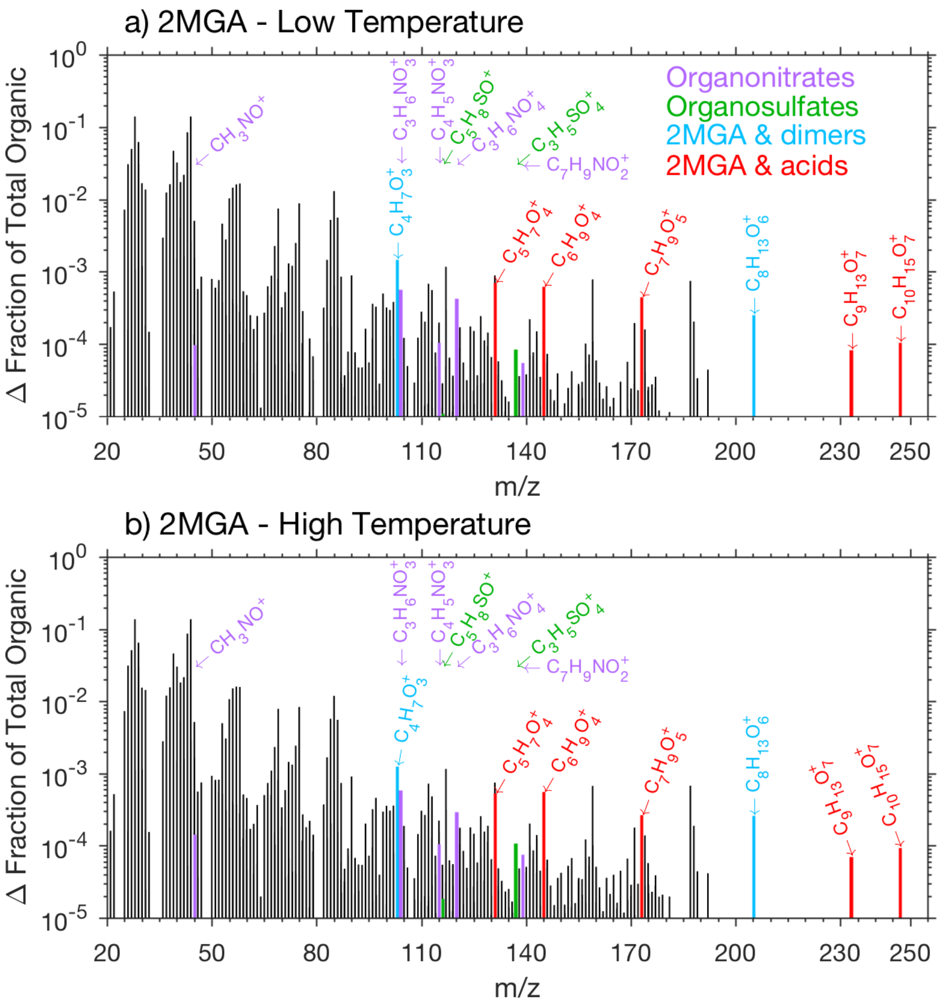

Figure S14. High resolution AMS mass spectra (averaged over 10h of photooxidation - the sulfate background) for experiment M4 (13 °C, panel a) and M5 (32 °C, panel b). Fragments are labeled as 2-MGA monomer/dimer (**cyan**), esterification of 2-MGA with acids (**red**), examples of organosulfate fragments (**dark green**), and examples of organonitrate fragments - $C_xH_yNO_z$ (**purple**).

References

Charan, S. M., Kong, W., Flagan, R. C., and Seinfeld, J. H.: Effect of particle charge on aerosol dynamics in Teflon environmental chambers, Aerosol Sci. Technol., 52:8, 854–871, https://doi.org/10.1080/02786826.2018.1474167, 2018.

Crump, J. G. and Seinfeld, J. H.: Turbulent deposition and gravitational sedimentation of an aerosol in a vessel of arbitrary shape, J. Aerosol Sci., 12, 405–415, https://doi.org/10.1016/0021-8502(81)90036-7, 1981.

Docherty, K. S., Jaoui, M., Corse, E., Jimenez, J. L., Offenberg, J. H., Lewandowski, M., and Kleindienst, T. E.: Collection efficiency of the aerosol mass spectrometer for chamber-generated secondary organic aerosols, Aerosol Sci. Technol., 47, 294–309, https://doi.org/10.1080/02786826.2012.752572, 2013.

Dommen, J., Metzger, A., Duplissy, J., Kalberer, M., Alfarra, M. R., Gascho, A., Weingartner, E., Prevot, A. S. H., Verheggen, B., and Baltensperer, U.: Laboratory observation of oligomers in the aerosol from isoprene/NO_x photooxidation, Geophys. Res. Lett., 33, L13 805, https://doi.org/10.1029/2006GL026523, 2006.

Farmer, D. K., Matsunaga, A., Docherty, K. S., Surratt, J. D., Seinfeld, J. H., Ziemann, P. J., and Jimenez, J. L.: Response of an aerosol mass spectrometer to organonitrates and organosulfates and implications for atmospheric chemistry, Proc. Natl. Acad. Sci. U. S. A., 107, 6670–6675, https://doi.org/10.1073/pnas.0912340107, 2010.

Leppa, J., Mui, W., Grantz, A. M., and Flagan, R. C.: Charge distribution uncertainty in differential mobility analysis of aerosols, Aerosol Sci. Technol., 51, 1168–1189, https://doi.org/10.1080/02786826.2017.1341039, 2017.

Lopez-Yglesias, X. and Flagan, R. C.: Ion–aerosol flux coefficients and the steady-state charge distribution of aerosols in a bipolar ion environment, Aerosol Sci. Technol., 47, 688–704, https://doi.org/10.1080/02786826.2013.783684, 2013.

Nah, T., McVay, R. C., Pierce, J. R., Seinfeld, J. H., and Ng, N. L.: Constraining uncertainties in particle-wall deposition correction during SOA formation in chamber experiments, Atmos. Chem. Phys., 17, 2297–2310, https://doi.org/10.5194/acp-17-2297-2017, 2017.

Pieber, S. M., Haddad, I. E., Slowik, J. G., Canagaratna, M. R., Jayne, J. T., Platt, S. M., Bozzetti, C., Daellenbach, K. S., Frohlich, R., Vlachou, A., Klein, F., Dommen, J., Miljevic, B., Jimenez, J. L., Worsnop, D. R., Baltensperger, U., and Prevot, A. S. H.: Inorganic salt interference on CO_2^+ in Aerodyne AMS and ACSM organic aerosol composition studies, Environ. Sci. Technol., 50, 10 494–10 503, https://doi.org/10.1021/acs.est.6b01035, 2016.

Sunol, A. M., Charan, S. M., and Seinfeld, J. H.: Computational simulation of the dynamics of secondary organic aerosol formation in an environmental chamber, Aerosol Sci. Technol., 52, 470–482, https://doi.org/10.1080/02786826.2018.1427209, 2018.

Wiedensohler, A.: An approximation of the bipolar charge distribution for particles in the submicron size range, J. Aerosol Sci., 19, 387–389, https://doi.org/10.1016/0021-8502(88)90278-9, 1988.

Zhang, H., Surratt, J. D., Lin, Y. H., Bapat, J., and Kamens, R. M.: Effect of relative humidity on SOA formation from isoprene/NO photooxidation: Enhancement of 2-methylglyceric acid and its corresponding oligoesters under dry conditions, Atmos. Chem. Phys., 11, 6411–6424, https://doi.org/10.5194/acp-11-6411-2011, 2011.